Zhbanov *et al.*
Micro and Nano Systems Letters (2023) 11:11
https://doi.org/10.1186/s40486-023-00175-w

Micro and Nano Systems Letters

REVIEW

Open Access

Current status and further development of deterministic lateral displacement for micro-particle separation

Alexander Zhbanov[1], Ye Sung Lee[1] and Sung Yang[1,2*]

Abstract

Deterministic lateral displacement (DLD) is a passive, label-free, continuous-flow method for particle separation. Since its discovery in 2004, it has been widely used in medical tests to separate blood cells, bacteria, extracellular vesicles, DNA, and more. Despite the very simple idea of the DLD method, many details of its mechanism are not yet fully understood and studied. Known analytical equations for the critical diameter of separated particles include only the gap between the columns in the DLD array and the fraction of the column shift. The dependence of the critical diameter on the post diameter, channel height, and a number of other geometric parameters remains unexplored. The problems also include the effect of flow rate and particle concentration on the critical diameter and separation efficiency. At present, DLD devices are mainly developed through numerical simulation and experimental validation. However, it is necessary to find fundamental regularities that would help to improve the separation quantitatively and qualitatively. This review discusses the principle of particle separation, the physical aspects of flow formation, and hydrodynamic forces acting on particles in DLD microchannels. Various analytical models of a viscous flow in an array of cylindrical posts are described. Prospects for further research are outlined.

Keywords Microfluidics, Deterministic lateral displacement, Particle separation, Critical particle diameter

Introduction

Sorting, separating, isolating, and detecting microparticles are important for a wide range of applications, from chemical processing to clinical diagnostics [1]. Advances in microfluidics have led to revolutionary progress in this field. The problems posed can be solved either with label-based or label-free approaches [2]. This review is devoted to label-free methods that use only the intrinsic properties of separated particles. Label-free microfluidic sorting is very promising for rapid blood testing and point-of-care blood diagnostics [3]. The separation of microparticles from a suspension can be carried out by active or passive methods [4, 5]. Passive methods utilize only hydrodynamic forces arising in microfluidic channels, while active methods additionally use external physical influences. Active methods include acoustophoresis, electrophoresis, dielectrophoresis, magnetophoresis, optical tweezers, and centrifugation. Passive methods rely on the size, shape, density, and deformability of particles (cells, molecules) and are represented by inertial microfluidics, pinched flow fractionation, hydrodynamic filtration, cross-flow filtration, deterministic lateral displacement, gravity-driven separation, viscoelastic microfluidics, and shear-induced diffusion [1, 6]. This review focuses on passive methods, namely, deterministic lateral displacement (DLD).

The DLD method was first published by Huang et al. [7]. Sturm et al. outlined the history of discovery from

*Correspondence:
Sung Yang
syang@gist.ac.kr
[1] School of Mechanical Engineering, Gwangju Institute of Science and Technology (GIST), Gwangju 61005, Republic of Korea
[2] Department of Biomedical Science and Engineering, Gwangju Institute of Science and Technology (GIST), Gwangju 61005, Republic of Korea

idea to implementation [8]. The DLD device divides particles into large and small in relation to the critical diameter and concentrates large particles. General advances in DLD are described in a number of recent reviews (e.g., [9, 10]). DLD has especially great potential for biomedical and clinical applications in the separation and isolation of biological micro-objects [11], blood cells [12], circulating tumor cells [13–21], leukocytes [22], single cells [23], extracellular vesicles [24–27], sub-micrometer particles [4], and nanoparticles [10, 28, 29].

For almost two decades, the DLD theory has continuously developed, various DLD devices have been designed, high efficiency and high-performance sorting of particles have been achieved, and the minimum critical diameter approached the nanometer scale. Nevertheless, many questions remain open despite the simple idea and relatively easy practical realization of DLD separation. The nature of the separation mechanisms is still not completely unclear; in particular, the interaction between particles and flow, particles and a microchannel, and between particles requires research. The influence of the microchannel geometry on separation efficiency is not fully understood and studied. The problems also include the effect of flow rate and particle concentration on the critical diameter and a number of others.

The purpose of the review is to identify key challenges that need to be tackled in order to improve the quality and performance of the DLD. The review focuses on the separation of rigid spherical particles on an array of cylindrical posts at a moderate Reynolds number.

Basic of DLD

Principle of separation

The cross-section of a typical DLD device along the median plane between the top and bottom of the channel is shown in Fig. 1, where the flow is directed from left to right. Here and below, the x-axis of the Cartesian coordinate system coincides with the flow. The y-axis is perpendicular to the x-axis and lies in the median plane. The pressure difference causes fluid to move through the array of cylindrical posts. The transverse period of the array (in the y-direction) is λ. The longitudinal period (in the x-direction) is λ^*. In most practical cases, $\lambda \approx \lambda^*$. The gap between posts is g. The cylindrical posts are shifted by $\varepsilon\lambda$ in each subsequent row so that the pattern is repeated after M shifts. Thus, the flux between two posts is divided into M flow streams with equivalent flow rates and $\varepsilon = 1/M$ (in Fig. 1, $M = 4$). Each stream flows in a zigzag path, from left to right on average. Separated particles are considered spherical and rigid. Small particles follow the same path as the streamlines in a zigzag mode.

Large particles whose radius exceeds the width of the first streamline β, travel in the bump mode (or displacement mode). The velocity profile in each gap between two posts is described by function $u(y)$.

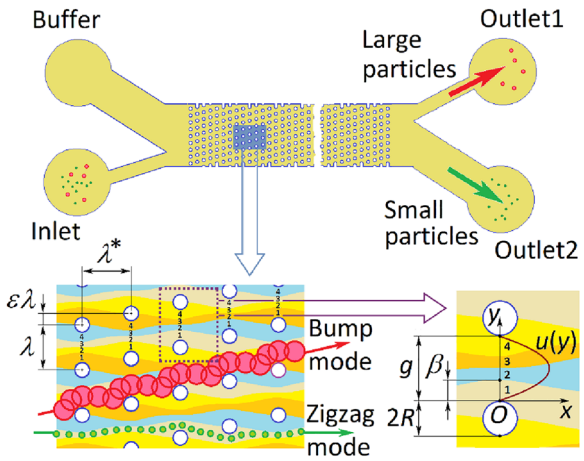

Fig. 1 Top view of the median plane of a typical sorting device and the principal of deterministic lateral displacement (DLD)

The flow rate equivalence in each streamline is expressed by

$$\int_0^{\beta} u(y)dy = \varepsilon \int_0^{g} u(y)dy. \tag{1}$$

Usually, it is assumed that the center of a rigid spherical particle moves strictly along the streamline. If the particle collides with the post, it goes around this obstacle due to mechanical contact and fluid flow. Therefore, the flow is characterized by a very low Reynolds number. Under these assumptions, the solution of Eq. (1) for β gives the critical particle diameter $D_c = 2\beta$. To calculate the width β and the critical diameter D_c, the velocity profile $u(y)$ should be found. The velocity profile depends on the flow regime in the microfluidic channel.

Characterization of flow regimes

DLD devices operate at a constant flow rate or pressure drop for an extended period of time so that a steady-state flow regime is established.

Typical microchannel sizes, fluid properties, and particle parameters are shown in Table 2 (see Appendix) along with a list of designations. These data are used below for estimating flow regimes, velocity profiles, and forces acting on particles.

The Reynolds number (Re) is the ratio of fluid momentum force to viscous shear force for a flowing fluid. The channel Reynolds number (Re_C) is expressed as follows [30]

$$Re_C = \frac{\rho_f U_{Max} D_H}{\mu_f}. \quad (2)$$

Here ρ_f is the fluid density, μ_f is the fluid viscosity, U_{Max} is the maximum velocity of the fluid, and D_H is the hydraulic diameter of the channel, defined as

$$D_H = \frac{4A}{P}, \quad (3)$$

where A and P are the area and perimeter of the channel cross-section, respectively.

Fluid moves in the channel with the average velocity $U_{Ave} = Q/A$, where Q is the volume flow rate, $A = Wh$ is the cross-section area, and W and h are the total width and height of the channel, respectively. The fluid velocity is maximum approximately in the middle of the gap between the posts. Using the assumption that velocity profile $u(y)$ is parabolic, the maximum velocity is

$$U_{Max} = \frac{3U_{Ave}\lambda}{2g}. \quad (4)$$

Calculations give U_{Ave}=0.0521 m s^{-1} and U_{Max}=0.130 m s^{-1}. Using Eq. (3), the hydraulic diameter of the gap between two posts $D_H = 2gh/(g+h) = 24$ μm. According to Eq. (2), the channel Reynolds number Re_C=3.13. This value belongs to the moderate Reynolds number regime ($Re_C \lesssim 18$) [31] and indicates a stable laminar flow in the channel. Dincau et al. [31] stated that there is a lack of comprehensive studies of microscale DLD performance in high and moderate Reynolds number regimes.

Estimation of critical diameter

Inglis et al. [32] greatly simplified the problem and assumed that the flow in the gap between two posts is the plane Poiseuille flow of a viscous fluid between two parallel plates separated by a distance g with no-slip boundary conditions.

The parabolic velocity profile $u(y)$ is shown in Fig. 1. Using this profile, Inglis et al. [32] solved Eq. (1) for β and found the critical diameter (Inglis diameter):

$$D_C^{Inglis} = 2\beta_{Inglis} = g\left(1 + 2w + \frac{1}{2w}\right), \quad (5)$$

where $w = \left[\frac{1}{8} - \frac{\varepsilon}{4} + \sqrt{\frac{\varepsilon}{16}(\varepsilon - 1)}\right]^{(1/3)} \left(-\frac{1}{2} - \mathrm{j}\frac{\sqrt{3}}{2}\right)$ and j is the imaginary unit $\mathrm{j} = \sqrt{-1}$.

Equation (5) predicts the particle separation into the zigzag and bumping mode but gives an underestimated critical diameter.

Davis et al. [33, 34] separated particles in many devices with different row shift fractions and gaps and found the following empirical formula for critical diameter (Davis diameter):

$$D_C^{Davis} = 1.4g\varepsilon^{0.48}. \quad (6)$$

For the parameters given in Table 2, $D_C^{Inglis} = 8.12$ μm and $D_C^{Davis} = 9.97$ μm. Equation (6) is considered more accurate and is often used for the preliminary design of DLD devices.

The well-known Inglis and Davis diameters explicitly depend only on the gap (g) and shift fraction (ε). Dependence on the post radius (R) and transverse period (λ) is implicit since $g = \lambda - 2R$.

It seems clear that the critical diameter also depends on the post radius, the longitudinal period, the channel height, as well as the flow rate, and the particle density. However, to the best of our knowledge, such analytical dependences are absent in the literature. In most cases, dependences of this kind are studied numerically.

In addition to the usual post template ($\lambda \approx \lambda^*$, see Fig. 2A), so-called asymmetrical DLD gaps [35] or doubly-periodic arrays [36] are possible ($\lambda < \lambda^*$ and $\lambda > \lambda^*$, see Fig. 2B, C). Zeming et al. [35] found that in both cases $\lambda < \lambda^*$ and $\lambda > \lambda^*$ the critical diameter decreases compared to the conventional geometry $\lambda \approx \lambda^*$, which enhances the separation resolution and throughput. Koens et al. [36] state that a slow viscous flow through a doubly-periodic system has no analytical solution. The rotated array layout was also studied [9] (see Fig. 2D).

The shape of the posts significantly affects the separation of particles (Fig. 3).

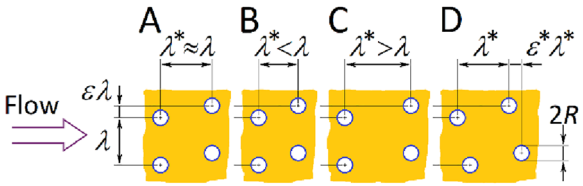

Fig. 2 Periodical structures of DLD arrays

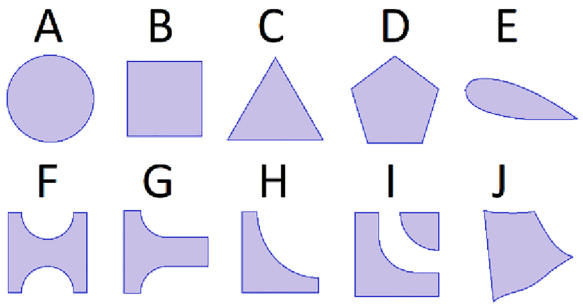

Fig. 3 Various types of posts

In addition to circular posts (Fig. 3A), various other posts have been investigated: square [37, 38] (Fig. 3B), triangular [13, 38–40] (Fig. 3C), polygonal [39] (Fig. 3D), airfoil [41] (Fig. 3E), I-shaped [37, 42] (Fig. 3F), T-shaped [42] (Fig. 3G), L-shaped [43] (Fig. 3H), L°-shaped [44] and others. Hyun et al. [45] used topology-optimized posts instead of cylindrical ones (Fig. 3J).

Zhang et al. [38] modeled posts in the shape of a circle, square, rhombus, and triangle, and generalized Eq. (2)

$$D_C^{Zhang} = \xi g \varepsilon^{\zeta}. \tag{7}$$

where ξ and ζ are dimensionless geometric coefficients for different post shapes. They encountered difficulties in determining the critical diameter of deformable particles.

High-throughput of DLD devices

One of the main disadvantages of DLD is its low throughput due to tiny volume [23]. The DLD throughput can be increased in three ways: by parallelizing the microchannel, by increasing the flow velocity, and by increasing the channel height.

Liu et al. [15] connected eight parallel channels into one single chamber, achieving a flow rate of 9.6 mL min^{-1}. Smith et al. [25] integrated 1024 nanoscale DLD arrays on a single chip. The achieved flow rate of 900 μL h^{-1} is high for separating nanometer-size particles. Integration of multiple arrays requires a high-tech fabrication while the principle of DLD remains the same, as first reported by Huang et al. [7].

Dincau et al. [31] studied the high Reynolds number regime ($10 < Re < 60$) through numerical simulation and experimental validation to achieve high throughput. The maximum fluid velocity in the channel was about 1.6 m s^{-1} at $Re = 60$. They demonstrated the formation of vortices behind the cylindrical posts, which, together with posts, create a virtual hydrodynamic shape resembling airfoils. Dincau et al. showed a decrease in the critical diameter as the Reynolds number increases.

The throughput increases proportionately to the channel height at a constant average fluid velocity. Bae et al. [46] investigated the effect of channel height on the critical particle diameter. They showed that the critical particle diameter depends on the height position of the particle. The fabrication of a channel with high posts encounters technological difficulties. The most common material for DLD device fabrication is polydimethylsiloxane (PDMS). In the case of PDMS, the tall posts are very flexible, and it is necessary to find another material and develop an alternative manufacturing technique.

Table 1 gives a summary of reviewed DLD devices for micro-particle separation and concentration. This table presents particle sizes and nature, flow rate ranges, and device efficiencies. The summary provides insight into various DLD devices that serve different purposes and separate a wide range of particles under different initial conditions.

The weak point of DLD devices is the inability to adjust the critical diameter during operation. The critical diameter depends on many parameters, so the DLD design should focus on the physical processes between the posts.

Forces acting on the particle

Characterization of particle motion

The particle Reynolds number (Re_p) is defined as [30]:

$$Re_P = Re_C \left(\frac{D_P}{D_H}\right)^2 = \frac{\rho_f U_{Max} D_P^2}{\mu_f D_H}. \tag{8}$$

where D_P is the particle diameter. Using the parameters given in Table 2, the particle Reynolds number $Re_P = 0.542$. The inertial focusing of particles occurs when the particle Reynolds number $Re_p \geq 1$ [1, 47]. Thus, shear-induced and wall-induced lift forces have little effect on particles in DLD devices at a moderate channel Reynolds number.

The particle moves in the DLD array along a winding trajectory resembling movement in a serpentine channel. The dimensionless Dean number (De) expresses the ratio of the transverse fluid flow arising due to the curvature of the channel to the longitudinal flow [30]:

$$De = Re_C \left(\frac{D_H}{2R_C}\right)^{1/2}, \tag{9}$$

where R_C is the radius of the channel curvature. The assumption that the radius of the channel curvature is equal to the post radius ($R_C = R$) gives an upper bound of the Dean number, $De = 3.43$. A low Dean number ($De < 40$–60) indicates that the flow is completely unidirectional and secondary flows do not occur when the fluid direction changes [48].

Characterization of forces

The hydrodynamic forces acting on a particle can be compared to the Stokes drag force (F_D) acting on a stationary particle

$$F_D = 3\pi \mu_f D_P U_{Max}. \tag{10}$$

Substitution of values from Table 2 gives $F_D = 12.3$ nN. If the particle moves at the fluid velocity, then $F_D = 0$.

As particles flow in the microchannel, they experience shear gradient lift force (F_S) and wall interaction lift force (F_W), which are expressed as [1, 30, 47]:

Table 1 Summary of microfluidic platforms for DLD micro-particle separation

Post shape	Throughput/flow rate/Reynolds number	Sample type	Efficiency/recovery/remarks	References
Circular posts	Average fluid velocity (U_{Ave}) ~ 400 μm s^{-1}	Separation from a mixture of 0.80, 0.90, and 1.03 μm beads/focusing and sorting of two bacterial artificial chromosome DNAs with 61 and 158 kb in size	Resolution of ~ 10 nm	[7]
Triangular posts	Flow rate (Q) up to 10 mL min^{-1}	Separation of 15–30 μm large circulating tumor cells (CTCs) from blood	Recovery rate of 85%	[13]
Circular posts	Maximum throughput 10 mL min^{-1} with 5 parallel channels	Separation of cancer cells (MCF-7, KYSE150, MDAMB231, A549, and HEPG2)	The efficiency of sorting at a speed of 2 mL min^{-1} is higher than 80%	[14]
Mirrored triangular micropost array	Throughput of 9.6 mL min^{-1}	CTCs isolation (MCF-7) from spiked blood samples	90% capture and more than 50% capture purity at cell concentration 10^2 cells mL^{-1}	[15]
Circular posts	Flow rates (Q) 7 μL min^{-1} (for specimen) and 190 μL min^{-1} (for buffer)	CTCs in tumor-bearing mouse	Enrichment of tumor cells to 0.05% from the blood, in which CTCs were negligibly detected among three million blood cells	[16]
Circular and asymmetric posts	Flow rate (Q) 0.5 mL h^{-1}	CTCs cluster separation from whole blood	99% recovery of large clusters, over 87% cell viabilities	[17]
Circular posts/Cascaded DLD modules	Flow rate (Q) 200 μL min^{-1} (for DLD #1) and 30 μL min^{-1} (for DLD #2)	Extraction of *E. coli* bacteria from blood samples spiked with prostate cancer cells	Depletion yield of 100% for cancer cells and 93% for red blood cells (RBCs)	[22]
Circular posts	Flow rate (Q) 3.74 mL h^{-1}	Cancer-cell-derived (BxPC-3 cells) extracellular vesicles	Recovery efficiency of 39% with purity of 98.5%	[24]
Circular posts/Integrate 1024 nano-DLD devices	Parallel processing sample flow rate (Q) up to 900 μL h^{-1}	Extracellular vesicles/exosomes isolation from serum and urine samples (30–200 nm)	Up to 60-fold concentration Recovery 50%	[25]
Circular nano-DLD array with a 25–235 nm gap	Flow rate (Q) 0.1–0.2 nL min^{-1}/Velocity (u) 200–300 μm s^{-1}	Separation of 20 to 110 nm beads and exosomes	Up to 100% separation	[28]
Circular posts	High-Re regime ($10 < Re < 60$) /Flow rate (Q) 14 mL min^{-1}	Polystyrene beads (10, 15, and 20 μm)		[31]
Circular posts	Average bead velocity 500–1500 μm s^{-1}	Polystyrene beads ranging from 2.3 to 22 μm		[32]
Circular posts	Reynolds number $Re < 1$/Velocity (u) ≤ 0.1 cm s^{-1}/flow rate (Q) ~ 1 μL min^{-1}	Separation of blood plasma from the blood cells (white, red, and platelets)	100% recovery	[33]
Circular posts	Flow rate (Q) 0.5 μL min^{-1}	Polystyrene beads/RBCs separation	91.2% separation index	[35]
I-shape, circular, and square posts	Flow rate (Q) 0.2 μL min^{-1} (for diluted blood sample) and 0.5 μL min^{-1} (for PBS buffer stream)	Polystyrene beads /RBCs/*E. coli*	100% separation of RBCs from blood samples	[37]
Circular and triangular pillars	Particle average velocity (v) from 0.1 to 4.5 mm s^{-1}	Polystyrene beads from 1.9 to3.8 μm		[39]
Triangular posts/Coupling of inertial microfluidics and DLD	Flow rate (Q) 40–400 μL min^{-1}	Polystyrene particles (7 and 15 μm), cancer cells (MCF-7), human whole blood	Separation efficiency of over 99.9% and a target sample purity of 93.59%	[40]
Airfoil posts	Reynolds number Re up to 100	Separation from a mixture of 10, 15, and 20 μm beads	Efficiency of 75% (for 10 μm), 83% (for 15 μm), and 100% (for 20 μm beads)	[41]

Table 1 (continued)

Post shape	Throughput/flow rate/Reynolds number	Sample type	Efficiency/recovery/remarks	References
Arrays of I-shape, anvil shape, T-shape, L-shape, and circular posts	Flow rate (Q) 0.2 µL min^{-1} (for RBC sample) and 0.1 µL min^{-1} (for bacterial samples)	Disc-shaped RBCs/Rod-shaped *E. coli* (~ 0.50 µm wide and ~ 2.0 µm long) /Spherical *S. epidermidis* (~ 0.7 µm) /Rod-shaped *K. pneumoniae* (~ 0.6 µm and ~ 1.8 µm) /Rod-shaped *P. aeruginosa* (~ 0.6 µm and ~ 1.6 µm)	100% separation	[42]
Circular and inverse L-shape	Flow rate (Q) 0.8 mL min^{-1}	RBCs	Purity 97.4% (RBCs)	[43]
L^{o}-shaped posts/cascaded filter-DLD chip	Flow rate (Q) 1 mL min^{-1}	Isolation of CTCs	Purity 99.995%	[44]
Topology-optimized posts	Flow rate (Q) 6500 µL h^{-1}	Polystyrene beads 2–6.5-µm	Separation efficiency 92.2%	[45]

$$F_S = C_S \rho_f U_{Max}^2 \frac{D_P^3}{D_H}, \tag{11}$$

$$F_W = C_W \rho_f U_{Max}^2 \frac{D_P^6}{D_H^4}, \tag{12}$$

where C_S and C_W are the lift coefficients for the shear gradient force and the wall interaction force, respectively. The lift coefficients C_S and C_W vary with the Reynolds number and particle position. Calculations using Table 2 give $F_S = 0.352$ nN and $F_W = 0.0255$ nN. The lift forces are comparable to drag forces, so they must be taken into account when designing DLD devices.

The inertia of a particle moving along a curved path causes a centrifugal force (F_C) [49]:

$$F_C = (\rho_p - \rho_f) \frac{\pi D_P^3}{6 R_C} U_{Max}^2, \tag{13}$$

The assumption that the curvature radius is equal to the post radius ($R_C = R$) gives $F_C = 0.0885$ nN.

Analytical models of fluid flow

Flow between two parallel plates

The plane Poiseuille flow of a viscous fluid is pressure-induced flow created between two infinitely long parallel plates (see Fig. 4B). In this problem, the Navier–Stokes equations are reduced to a linear ordinary differential equation of the second order with respect to the y-component of the velocity u:

$$\mu_f \frac{d^2 u}{dy^2} = \frac{dp}{dx}. \tag{14}$$

where p is the pressure. The pressure gradient is constant, $dp/dx = \text{const}$. The y-component of velocity is zero at the channel walls. The resulting analytical solution to Eq. (5) is given as

$$u(y) = -\frac{dp}{dx} \frac{1}{2\mu} y(g - y). \tag{15}$$

The y-component of the velocity v equals zero, $v = 0$.

The parabolic velocity profile (15) was used to solve Eq. (1) and determine the Inglis critical diameter (5).

Poiseuille flow in rectangular pipes

The flow in a rectangular pipe is a more realistic model of flow in the gap between two posts (see Fig. 4B). The analytical solution of the Poiseuille flow in the rectangular pipe over range $-a \le y \le a$ and $-b \le z \le b$ is expressed as follows [50, 51]:

$$u(y,z) = \frac{16a^2}{\mu_f \pi^3} \left(-\frac{dp}{dx}\right) \sum_{n=1,3,5....}^{\infty} (-1)^{(n-1)/2} \left[1 - \frac{\cosh(n\pi z/2a)}{\cosh(n\pi b/2a)}\right] \frac{\cos(n\pi y/2a)}{n^3}, \tag{16}$$

where μ is the dynamic viscosity and p is the hydrostatic pressure.

Bae et al. [46] used Eq. (16) to numerically solve the following equation for β:

$$\int_{-a}^{-a+\beta} u(y, z = \text{const}) dy = \varepsilon \int_{-a}^{a} u(y, z = \text{const}) dy. \tag{17}$$

The solution shows that the critical diameter depends on the particle position in the channel along the z-coordinate, $D_C(z) = 2\beta(z)$. This conclusion was confirmed experimentally.

Flow perpendicular to array of cylinders, Happel's model

In addition to analytical solutions for fluid velocity in the y direction ("Flow between two parallel plates" section) and a two-dimensional velocity distribution in the y–z plane ("Poiseuille flow in rectangular pipes" section), solutions are also known for a two-dimensional velocity distribution in the x–y plane (see Fig. 5).

The flow field in an array of parallel cylinders oriented perpendicular to the flow direction at low Reynolds numbers has been studied for a long time. The periodic structure can be represented by a unit cell (see Fig. 5, Unit cell). This is a more accurate model than the flow between two parallel plates. In 1959, Happel [52] derived the stream function equation for such a system. Happel considered the cylinder array moves in a stationary liquid with a constant velocity (see Fig. 5, Happel's model).

The Stokes approximation for 2D steady motion takes the form of a biharmonic equation

$$\Delta^2 \Psi(r, \theta) = 0, \tag{18}$$

where Ψ is the stream function such that in cylindrical coordinates (r, θ) the velocity components (u_r, u_θ) are given by

$$u_r(r,\theta) = \frac{1}{r} \frac{\partial \Psi}{\partial \theta} \quad \text{and} \quad v_\theta(r,\theta) = -\frac{\partial \Psi}{\partial r}. \tag{19}$$

The vorticity ω is given by

$$\omega = \frac{\partial v_\theta}{\partial r} - \frac{1}{r} \frac{\partial u_r}{\partial \theta} + \frac{v_\theta}{r} = -\Delta \Psi, \tag{20}$$

$$\text{where} \quad \Delta = \frac{\partial^2}{\partial r^2} + \frac{1}{r} \frac{\partial}{\partial r} + \frac{1}{r^2} \frac{\partial^2}{\partial \theta^2}. \tag{21}$$

Happel assumed that the normal velocity and shear stress on the outer surface of the cylindrical shell are zero. The non-slip conditions are satisfied on the inner surface.

$$u_r = v_\theta = 0 \quad \text{at } r = a \tag{22}$$

and

$$u_r = U_{Max}\cos\theta, \quad \frac{\partial v_\theta}{\partial r} + \frac{1}{r}\frac{\partial u_r}{\partial \theta} - \frac{v_\theta}{r} = 0 \quad \text{at r = c}, \tag{23}$$

where c is the radius of the unit cell for the Happel's model.

A general solution to Eq. (18) is

$$\Psi = \sin\theta\left[\frac{1}{8}Cr^3 + \frac{1}{2}Dr\left(\ln r - \frac{1}{2}\right) + Er + \frac{F}{r}\right], \tag{24}$$

where C, D, E, and D are arbitrary constants that can be determined using boundary conditions (22) and (23). Under such conditions, the stream function is expressed as

$$\begin{aligned}\Psi = &\left\{A_1 r^3\left[1 - \frac{4\ln r}{2\ln R + 1}\left(\frac{R}{r}\right)^2 + \frac{2\ln R - 1}{2\ln R + 1}\left(\frac{R}{r}\right)^4\right]\right.\\ &\left.+B_1 R^2 r\left[1 - \frac{2\ln r}{2\ln R + 1} - \left(\frac{R}{r}\right)^2\frac{1}{2\ln R + 1}\right]\right\}\sin\theta\\ &+\sum_{n=2}^{N}\left\{A_n r^{2n+1}\left[1 - 2n\left(\frac{R}{r}\right)^{4n-2} + (2n-1)\left(\frac{R}{r}\right)^{4n}\right]\right.\\ &\left.+B_n R^2 r^{2n-1}\left[1 - (2n-1)\left(\frac{R}{r}\right)^{4n-4} + 2(n-1)\left(\frac{R}{r}\right)^{4n-2}\right]\right\}\sin(2n-1)\theta,\end{aligned} \tag{31}$$

$$\Psi(r,\theta) = \frac{1}{2}U_{Max}\sin\theta\left[\frac{\alpha^2}{(1+\alpha^2)} - \frac{1}{2}\ln\alpha - \frac{1}{2}\right]^{-1}\left[\frac{1}{(1+\alpha^2)r} - \frac{(1-\alpha^2)}{(1+\alpha^2)}r + 2r\ln r - \frac{\alpha^2}{(1+\alpha^2)}r^3\right] = 0, \tag{25}$$

where α is the volume fraction occupied by cylinders, $\alpha = R^2/c^2$.

Sangani and Acrivos model

Sangani and Acrivos [53] extended the Happel's model to the square unit cell (see Fig. 5, Model of Sangani and Acrivos). The Stokes flow is described by Eq. (18). The boundary conditions are

$$\Psi = \omega = 0 \quad \text{on AE}, \tag{26}$$

$$\frac{\partial\Psi}{\partial x} = \frac{\partial\omega}{\partial x} = 0 \quad \text{on ED and CB}, \tag{27}$$

$$\omega = 0, \quad \Psi = 1 \quad \text{on DC}, \tag{28}$$

$$\Psi = \frac{\partial\Psi}{\partial r} = 0 \quad \text{on BA}. \tag{29}$$

The solution for the vorticity is given by

$$\begin{aligned}\omega = &2\left[4A_1 r - (4A_1 + 2B_1)\frac{R^2}{r(2\ln R + 1)}\right]\sin\theta +\\ &+8\sum_{n=2}^{N}\sin(2n-1)\theta\left\{nA_n r^{2n-1} + (n-1)\right.\\ &\left.[2nA_n - (2n-1)B_n]\frac{R^{4n-2}}{r^{2n-1}}\right\},\end{aligned} \tag{30}$$

and the solution for the stream function is

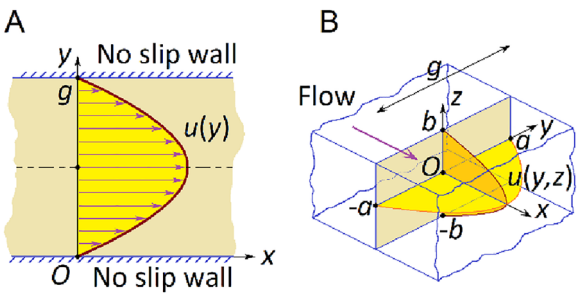

Fig. 4 Poiseuille flows between two parallel plates (**A**) and in square duct (**B**)

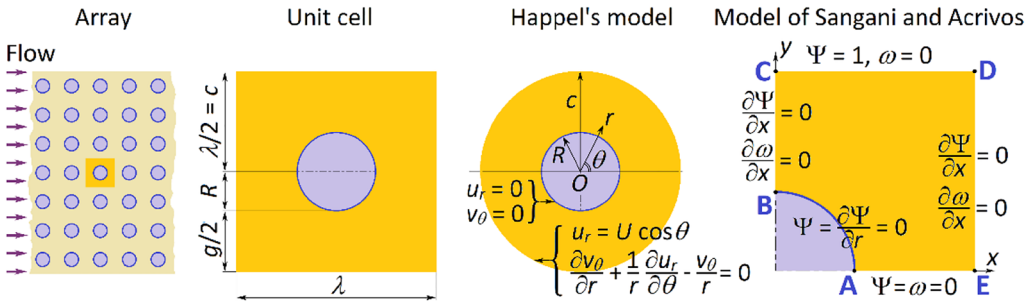

Fig. 5 Flow perpendicular to array of cylinders

where A_1, ..., A_n, B_1, ..., B_n are arbitrary constants determined by the boundary conditions. To find these constants, N points on the lines ED and DC are chosen, in which Eqs. (27) and (28) are to meet the boundary conditions. The boundary conditions on the lines AE and BA are satisfied automatically. Satisfaction of the boundary conditions at N points leads to forming a system of $2N$ linear algebraic equations. The arbitrary constants are determined by the solution of this system. Usually, $N=25–50$ is sufficient for a good approximation of the vorticity and stream function.

Numerical simulation and experimental verification

In most works, the authors used the following DLD device design strategy. First, they estimated the parameters of the DLD array using Eq. (6), the Davis diameter. Second, they carried out several iterations of numerical simulation and experimental verification to achieve satisfactory results. Thus, in all works, optimization was carried out, and, in one way or another, the influence of various parameters on the final result was studied.

However, only in a few works, any parameter was varied within wide limits to study the mechanism of its influence on the critical diameter and separation efficiency.

Beech [54] and Holm [55] studied the effect of channel height on the flow profile and critical diameter using 3D finite element modeling. Bae et al. [46] studied this effect by analytical methods and experimental verification. Additionally, Beech investigated the effect of post diameter on the flow profile when the device height and gap are kept constant. Kim et al. [56] numerically studied the post-size variation and developed detailed theories of DLD for nanometer particle focusing. Similar works should be carried out in the future.

Conclusions and perspectives

A review of the literature shows that deterministic lateral displacement remains a very attractive method for separating and sorting particles. Active development of more and more new devices continues. Increasing the throughput of devices and the efficiency of particle separation, the separation of micron and submicron particles, and the separation of highly concentrated particles and particles of similar sizes are challenging problems.

Therefore, the following tasks become important for the study:

1. A more detailed understanding of the DLD particle separation mechanism.
2. Influence of the post diameter, channel height, row and column shift fractions, and transverse and longitudinal periods of the posts array on the critical diameter.
3. Physical aspects of flow formation and the hydrodynamic forces acting on particles in DLD microchannels.
4. Effect of high flow rate and particle concentration on the critical diameter and separation efficiency.
5. Very accurate separation of close particle sizes.
6. Topology optimization of the post shape to reduce device clogging and improve separation efficiency.
7. Separation of soft and flexible particles of various shapes.

With the solution of these tasks, DLD will reveal its tremendous potential in the future.

Appendix

See Table 2.

Table 2 Nomenclature and typical values of DLD parameters

Notation	Description	Typical value	Units
A	Area of the channel cross-section	$\sim 32\times10^3$	μm^2
a	Half-width of the rectangular channel		
A_1, A_n, B_1, B_n	Arbitrary constants defined by boundary conditions		
B	Half-height of the rectangular channel		
C, D, E	Arbitrary constants defined by boundary conditions		
C_S	Lift coefficient for the shear gradient lift force	0.5	
C_W	Lift coefficient for the wall interaction force	0.5	
c	Radius of unit cell for the Happel's model		
D_C	Critical particle diameter		
$D_C^{Davis\ s}$	Critical diameter introduced by Davis et. al	~9.97	μm
D_C^{Inglis}	Critical diameter introduced by Inglis et. al	~8.12	μm
D_C^{Zhang}	Critical diameter introduced by Zhang et. al		
D_H	Hydraulic diameter of the channel	~24	μm
D_P	Particle diameter	10	μm
De	Dean number	~3.43	
F_C	Centrifugal force	~0.0885	nN
F_D	Stokes drag force	~12.3	nN
F_S	Shear gradient lift force	~0.352	nN
F_W	Wall interaction force	~0.0255	nN
g	Gap between the two posts	30	μm
h	Height of the channel	20	μm
j	Imaginary unit		
M	Whole number, period of the post array	20	
N	Number of terms in the series		
n	Summation index		
P	Perimeter of the channel cross-section		
p	Pressure		
Q	Volume flow rate in the microfluidic channel	6000	$\mu L\ h^{-1}$
r	Radial coordinate in cylindrical coordinates		
R	Radius of the cylindrical post	10	μm
R_C	Radius of the channel curvature		
Re_C	Channel Reynolds number	~3.13	
Re_P	Particle Reynolds number	~0.542	
U_{Ave}	Average fluid velocity in the channel	~0.0521	$m\ s^{-1}$
U_{Max}	Maximum fluid velocity in the channel	~0.130	$m\ s^{-1}$
u	x-velocity component		
$u(x)$, $u(x, y)$	Fluid velocity in the microchannel		
u_r	Radial velocity component		
v	y-velocity component		
v_θ	Angular velocity component		
W	Total width of the microfluidic channel	1600	μm
w	Auxiliary parameter for the Inglis diameter		
x, y, z	Cartesian coordinates		
α	Volume fraction occupied by cylindrical posts		
β	Width of the first streamline		
ε	Row shift fraction	0.05	
$\varepsilon*$	Column shift fraction		
λ	Transverse period of the post array	50	μm
$\lambda*$	Longitudinal period of the post array		

Table 2 (continued)

Notation	Description	Typical value	Units
μ_f	Fluid viscosity	1.0	mPa s
θ	Angular coordinate in cylindrical coordinates		
ρ_f	Fluid density	1000	kg m^{-3}
ρ_P	Particle density	1100	kg m^{-3}
ω	Vorticity		
ξ, ζ	Dimensionless geometric coefficients		
Ψ	Stream function		

The ~ sign means an estimated value

Acknowledgements
Not applicable.

Author contributions
AZ make contributions to the conception and design of the work and analysis and interpretation of data and have drafted the work; YSL make contributions to the conception and design of the work and substantively revised draft; SY supervised this research, evaluated and edited the manuscript. All authors read and approved the final manuscript.

Funding
This work was supported by a GIST Research Project grant funded by the GIST in 2023 and a National Research Foundation of Korea (NRF) grant funded by the Korean government (MSIT) (No. 2021R1A2C3008169).

Availability of data and materials
Not applicable.

Declarations

Ethics approval and consent to participate
Not applicable.

Competing interests
The authors declare that they have no competing interests.

Received: 26 June 2023 Accepted: 9 September 2023
Published online: 04 October 2023

References

1. Zhou J, Mukherjee P, Gao H, Luan Q, Papautsky I (2019) Label-free microfluidic sorting of microparticles. APL Bioeng 3:041504. https://doi.org/10.1063/1.5120501
2. Lee S, Kim H, Yang S (2023) Microfluidic label-free hydrodynamic separation of blood cells: recent developments and future perspectives. Adv Mater Technol 8:2201425. https://doi.org/10.1002/admt.202201425
3. Lu N, Tay HM, Petchakup C, He L, Gong L, Maw KK, Leong SY, Lok WW, Ong HB, Guo R, Li K, Ho H, Hou HW (2023) Label-free microfluidic cell sorting and detection for rapid blood analysis. Lab Chip 23:1226–1257. https://doi.org/10.1039/D2LC00904H
4. Zhang T, Hong Z-Y, Tang S-Y, Li W, Inglis DW, Hosokawa Y, Yalikun Y, Li M (2020) Focusing of sub-micrometer particles in microfluidic devices. Lab Chip 20:35–53. https://doi.org/10.1039/C9LC00785G
5. Zhang Y, Zheng T, Wang L, Feng L, Wang M, Zhang Z, Feng H (2021) From passive to active sorting in microfluidics: a review. Rev Adv Mater Sci 60:313–324. https://doi.org/10.1515/rams-2020-0044
6. Bayareh M (2020) An updated review on particle separation in passive microfluidic devices. Chem Eng Process 153:107984. https://doi.org/10.1016/j.cep.2020.107984
7. Huang LR, Cox EC, Austin RH, Sturm JC (2004) Continuous particle separation through deterministic lateral displacement. Science 304:987–990. https://doi.org/10.1126/science.1094567
8. Sturm JC, Cox EC, Comella B, Austin RH (2014) Ratchets in hydrodynamic flow: more than waterwheels. Interface Focus 4:20140054. https://doi.org/10.1098/rsfs.2014.0054
9. Salafi T, Zhang Y, Zhang Y (2019) A review on deterministic lateral displacement for particle separation and detection. Nano-Micro Lett 11:77. https://doi.org/10.1007/s40820-019-0308-7
10. Hochstetter A, Vernekar R, Austin RH, Becker H, Beech JP, Fedosov DA, Gompper G, Kim S-C, Smith JT, Stolovitzky G, Tegenfeldt JO, Wunsch BH, Zeming KK, Krüger T, Inglis DW (2020) Deterministic lateral displacement: challenges and perspectives. ACS Nano 14:10784–10795. https://doi.org/10.1021/acsnano.0c05186
11. Tang H, Niu J, Jin H, Lin S, Cui D (2022) Geometric structure design of passive label-free microfluidic systems for biological micro-object separation. Microsyst Nanoeng 8:62. https://doi.org/10.1038/s41378-022-00386-y
12. Catarino SO, Rodrigues RO, Pinho D, Miranda JM, Minas G, Lima R (2019) Blood cells separation and sorting techniques of passive microfluidic devices: from fabrication to applications. Micromachines 10:593. https://doi.org/10.3390/mi10090593
13. Loutherback K, D'Silva J, Liu L, Wu A, Austin RH, Sturm JC (2012) Deterministic separation of cancer cells from blood at 10 mL/min. AIP Adv 2:042107. https://doi.org/10.1007/s10404-010-0635-y
14. Liu Z, Huang F, Du J, Shu W, Feng H, Xu X, Chen Y (2013) Rapid isolation of cancer cells using microfluidic deterministic lateral displacement structure. Biomicrofluidics 7:11801. https://doi.org/10.1063/1.4774308
15. Liu Z, Zhang W, Huang F, Feng H, Shu W, Xu X, Chen Y (2013) High throughput capture of circulating tumor cells using an integrated microfluidic system. Biosens Bioelectron 47:113–119. https://doi.org/10.1016/j.bios.2013.03.017
16. Okano H, Konishi T, Suzuki T, Suzuki T, Ariyasu S, Aoki S, Hayase M (2015) Enrichment of circulating tumor cells in tumor-bearing mouse blood by a deterministic lateral displacement microfluidic device. Biomed Microdevices 17:59. https://doi.org/10.1007/s10544-015-9964-7
17. Au SH, Edd J, Stoddard AE, Wong KH, Fachin F, Maheswaran S, Haber DA, Stott SL, Kapur R, Toner M (2017) Microfluidic isolation of circulating tumor cell clusters by size and asymmetry. Sci Rep 7:2433. https://doi.org/10.1038/s41598-017-01150-3
18. Zhu S, Jiang F, Han Y, Xiang N, Ni Z (2020) Microfluidics for label-free sorting of rare circulating tumor cells. Analyst 145:7103–7124. https://doi.org/10.1039/D0AN01148G
19. Bayareh M, Mohammadali R, Usefian A (2021) Cancer cell separation using passive mechanisms: a review. Chall Nano Micro Scale Sci Technol 9:48–62. https://doi.org/10.22111/cnmst.2021.36975.1202
20. Kang H, Xiong Y, Ma L, Yang T, Xu X (2022) Recent advances in micro-/nanostructure array integrated microfluidic devices for efficient separation of circulating tumor cells. RSC Adv 12:34892–34903. https://doi.org/10.1039/D2RA06339E
21. Liu X, Ma L, Yan W, Aazmi A, Fang M, Xu X, Kang H, Xu X (2022) A review of recent progress toward the efficient separation of circulating tumor cells via micro-/nanostructured microfluidic chips. View 3:20210013. https://doi.org/10.1002/VIW.20210013

22. Pariset E, Parent C, Fouillet Y, François B, Verplanck N, Revol-Cavalier F, Thuaire A, Agache V (2018) Separation of biological particles in a modular platform of cascaded deterministic lateral displacement modules. Sci Rep 8:17762. https://doi.org/10.1038/s41598-018-34958-8
23. Hochstetter A (2020) Lab-on-a-chip technologies for the single cell level: separation, analysis, and diagnostics. Micromachines 11:468. https://doi.org/10.3390/mi11050468
24. Santana SM, Antonyak MA, Cerione RA, Kirby BJ (2014) Microfluidic isolation of cancer-cell-derived microvesicles from hetergeneous extracellular shed vesicle populations. Biomed Microdevices 16:869–877. https://doi.org/10.1007/s10544-014-9891-z
25. Smith JT, Wunsch BH, Dogra N, Ahsen ME, Lee K, Yadav KK, Weil R, Pereira MA, Patel JV, Duch EA, Papalia JM, Lofaro MF, Gupta M, Tewari AK, Cordon-Cardo C, Stolovitzky G, Gifford SM (2018) Integrated nanoscale deterministic lateral displacement arrays for separation of extracellular vesicles from clinically-relevant volumes of biological samples. Lab Chip 18(24):3913–3925. https://doi.org/10.1039/C8LC01017J
26. Meng Y, Asghari M, Aslan MK, Yilmaz A, Mateescu B, Stavrakis S, deMello AJ (2021) Microfluidics for extracellular vesicle separation and mimetic synthesis: recent advances and future perspectives. Chem Eng J 404:126110. https://doi.org/10.1016/j.cej.2020.126110
27. Havers M, Broman A, Lenshof A, Laurell T (2023) Advancement and obstacles in microfluidics-based isolation of extracellular vesicles. Anal Bioanal Chem 415:1265–1285. https://doi.org/10.1007/s00216-022-04362-3
28. Wunsch BH, Smith JT, Giford SM, Wang C, Brink M, Bruce RL, Austin RH, Stolovitzky G, Astier Y (2016) Nanoscale lateral displacement arrays for the separation of exosomes and colloids down to 20nm. Nat Nanotechnol 11:936–940. https://doi.org/10.1038/nnano.2016.134
29. Xie Y, Rufo J, Zhong R, Rich J, Li P, Leong KW, Huang TJ (2020) Microfluidic isolation and enrichment of nanoparticles. ACS Nano 14:16220–16240. https://doi.org/10.1021/acsnano.0c06336
30. Martel JM, Toner M (2014) Inertial focusing in microfluidics. Ann Rev Biomed Eng 16:371–396. https://doi.org/10.1146/annurev-bioeng-121813-120704
31. Dincau BM, Aghilinejad A, Hammersley T, Chen X, Kim J-H (2018) Deterministic lateral displacement (DLD) in the high Reynolds number regime: high-throughput and dynamic separation characteristics. Microfluid Nanofluid 22:59. https://doi.org/10.1146/10.1007/s10404-018-2078-9
32. Inglis DW, Davis JA, Austin RH, Sturm JC (2006) Critical particle size for fractionation by deterministic lateral displacement. Lab Chip 6:655–658. https://doi.org/10.1039/B515371A
33. Davis JA, Inglis DW, Morton KJ, Lawrence DA, Huang LR, Chou SY, Sturm JC, Austin RH (2006) Deterministic hydrodynamics: taking blood apart. Proc Natl Acad Sci USA 103:14779–14784. https://doi.org/10.1073/pnas.0605967103
34. Davis JA (2008) Microfluidic separation of blood components through deterministic lateral displacement. Ph.D. Thesis, Princeton University
35. Zeming KK, Salafi T, Chen C-H, Zhang Y (2016) "Asymmetrical deterministic lateral displacement gaps for dual functions of enhanced separation and throughput of red blood cells. Sci Rep 6:22934. https://doi.org/10.1038/srep22934
36. Koens L, Vernekar R, Krueger T, Lisicki M, Inglis DW (2023) The slow viscous flow around doubly-periodic arrays of infinite slender cylinders. arXiv:2301.12774. https://doi.org/10.48550/arXiv.2301.12774
37. Zeming KK, Ranjan S, Zhang Y (2013) Rotational separation of non-spherical bioparticles using I-shaped pillar arrays in a microfluidic device. Nat Commun 4:1625. https://doi.org/10.1038/ncomms2653
38. Zhang Z, Henry E, Gompper G, Fedosov DA (2015) Behavior of rigid and deformable particles in deterministic lateral displacement devices with different post shapes. J Chem Phys 143:243145. https://doi.org/10.1063/1.4937171
39. Loutherback K, Chou KS, Newman J, Puchalla J, Austin RH, Sturm JC (2010) Improved performance of deterministic lateral displacement arrays with triangular posts. Microfluid Nanofluid 9:1143–1149. https://doi.org/10.1007/s10404-010-0635-y
40. Xiang N, Wang J, Li Q, Han Y, Huang D, Ni Z (2019) Precise size-based cell separation via the coupling of inertial microfluidics and deterministic lateral displacement. Anal Chem 91:10328–10334. https://doi.org/10.1021/acs.analchem.9b02863
41. Dincau BM, Aghilinejad A, Chen X, Moon SY, Kim JH (2018) Vortex-free high-Reynolds deterministic lateral displacement (DLD) via airfoil pillars. Microfluid Nanofluid 22:137. https://doi.org/10.1007/s10404-018-2160-3
42. Ranjan S, Zeming KK, Jureen R, Fisher D, Zhang Y (2014) DLD pillar shape design for efficient separation of spherical and non-spherical bioparticles. Lab Chip 14:4250–4262. https://doi.org/10.1039/C4LC00578C
43. Zeming KK, Sato Y, Yin L, Huang N-J, Wong LH, Loo HL, Lim YB, Lim CT, Chen J, Preiser PR, Han J (2020) Microfluidic label-free bioprocessing of human reticulocytes from erythroid culture. Lab Chip 20:3445–3460. https://doi.org/10.1039/C9LC01128E
44. Liu Z, Huang Y, Liang W, Bai J, Feng H, Fang Z, Tian G, Zhu Y, Zhang H, Wang Y, Liu A, Chen Y (2021) Cascaded filter deterministic lateral displacement microchips for isolation and molecular analysis of circulating tumor cells and fusion cells. Lab Chip 21:2881–2891. https://doi.org/10.1039/D1LC00360G
45. Hyun J-C, Hyun J, Wang S, Yang S (2016) Improved pillar shape for deterministic lateral displacement separation method to maintain separation efficiency over a long period of time. Sep Purif Technol 172:258–267. https://doi.org/10.1016/j.seppur.2016.08.023
46. Bae JH, Zhbanov A, Yang S (2022) Effect of channel height on the critical particle diameter in a deterministic lateral device. Micro Nano Syst Lett 10:20. https://doi.org/10.1186/s40486-022-00163-6
47. Amini H, Lee W, Di Carlo D (2014) Inertial microfluidic physics. Lab Chip 14:2739–2761. https://doi.org/10.1039/C4LC00128A
48. Nazari N, Yun W, Kovscek AR (2023) The motion of long bubbles in microchannels using a meter-long, rectangular capillary on a chip. J Colloid Interface Sci 638:149–160. https://doi.org/10.1016/j.jcis.2023.01.073
49. Zhang J, Li W, Li M, Alici G, Nguyen N-T (2014) Particle inertial focusing and its mechanism in a serpentine microchannel. Microfluid Nanofluid 17:305–316. https://doi.org/10.1007/s10404-013-1306-6
50. White FM, Majdalani J (2022) Viscous fluid flow, 4th edn. McGraw-Hill Companies Inc, New York
51. Fukuchi T (2011) Numerical calculation of fully-developed laminar flows in arbitrary cross-sections using finite difference method. AIP Adv 1:042109. https://doi.org/10.1063/1.3652881
52. Happel J (1959) Viscous flow relative to arrays of cylinders. AIChE J 5:174–177. https://doi.org/10.1002/aic.690050211
53. Sangani AS, Acrivos A (1982) Slow flow past periodic arrays of cylinders with application to heat transfer. Int J Multiph Flow 8:193–206. https://doi.org/10.1016/0301-9322(82)90029-5
54. Beech JP (2011) Microfuidics separation and analysis of biological particles. Lund University: Lund. https://lup.lub.lu.se/record/2198801
55. Holm S (2018) Microfuidic cell and particle sorting using deterministic lateral displacement. Department of physics. Lund University, Lund. https://lup.lub.lu.se/record/bc57504b-5349-4a1a-8283-5eee9343c80e
56. Kim S-C, Wunsch BH, Hu H, Smith JT, Austin RH, Stolovitzky G (2017) Broken flow symmetry explains the dynamics of small particles in deterministic lateral displacement arrays. Proc Nat Acad Sci USA 114:E5034–E5041. https://doi.org/10.1073/pnas.1706645114

Publisher's Note